The Astrophysical Journal, 752:81 (13pp), 2012 June 20 doi:10.1088/0004-637X/752/2/81

Spitzer/MIPS 24 μm OBSERVATIONS OF HD 209458b: THREE ECLIPSES, TWO AND A HALF TRANSITS, AND A PHASE CURVE CORRUPTED BY INSTRUMENTAL SENSITIVITY VARIATIONS

Ian J. M. Crossfield[1], Heather Knutson[2], Jonathan Fortney[3,7], Adam P. Showman[4], Nicolas B. Cowan[5,8], and Drake Deming[6]
[1] Department of Physics, & Astronomy, University of California, Los Angeles, CA 90095, USA; ianc@astro.ucla.edu
[2] Caltech Division of Geological and Planetary Sciences, Pasadena, CA 91125, USA
[3] Department of Astronomy and Astrophysics, University of California, Santa Cruz, CA 95064, USA
[4] Department of Planetary Sciences and Lunar and Planetary Laboratory, The University of Arizona, Tucson, AZ 85721, USA
[5] Center for Interdisciplinary Exploration and Research in Astrophysics (CIERA) and Department of Physics & Astronomy, Northwestern University, Evanston, IL 60208, USA
[6] Department of Astronomy, University of Maryland, College Park, MD 20742, USA
Received 2012 February 7; accepted 2012 April 11; published 2012 May 29

ABSTRACT

We report the results of an analysis of all *Spitzer*/MIPS 24 μm observations of HD 209458b, one of the touchstone objects in the study of irradiated giant planet atmospheres. Altogether, we analyze two and a half transits, three eclipses, and a 58 hr near-continuous observation designed to detect the planet's thermal phase curve. The results of our analysis are: (1) a mean transit depth of $1.484\% \pm 0.033\%$, consistent with previous measurements and showing no evidence of variability in transit depth at the 3% level. (2) A mean eclipse depth of $0.338\% \pm 0.026\%$, somewhat higher than that previously reported for this system; this new value brings observations into better agreement with models. From this eclipse depth we estimate an average dayside brightness temperature of 1320 ± 80 K; the dayside flux shows no evidence of variability at the 12% level. (3) Eclipses in the system occur 32 ± 129 s earlier than would be expected from a circular orbit, which constrains the orbital quantity $e \cos \omega$ to be 0.00004 ± 0.00033. This result is fully consistent with a circular orbit and sets an upper limit of 140 m s^{-1} (3σ) on any eccentricity-induced velocity offset during transit. The phase curve observations (including one of the transits) exhibit an anomalous trend similar to the detector ramp seen in previous *Spitzer*/IRAC observations; by modeling this ramp we recover the system parameters for this transit. The long-duration photometry which follows the ramp and transit exhibits a gradual $\sim$0.2% decrease in flux over $\sim$30 hr. This effect is similar to that seen in pre-launch calibration data taken with the 24 μm array and is better fit by an instrumental model than a model invoking planetary emission. The large uncertainties associated with this poorly understood, likely instrumental effect prevent us from usefully constraining the planet's thermal phase curve. Our observations highlight the need for a thorough understanding of detector-related instrumental effects on long timescales when making the high-precision mid-infrared measurements planned for future missions such as *EChO*, *SPICA*, and the *James Webb Space Telescope*.

Key words: eclipses – infrared: planetary systems – planetary systems – planets and satellites: individual (HD 209458b) – stars: individual (HD 209458) – Sun: fundamental parameters – techniques: photometric

Online-only material: color figures

1. INTRODUCTION

Most known extrasolar planets were discovered via the radial velocity technique, in which the Doppler wobble of a star indicates an orbiting planet, and/or by the transit method, in which periodic dimming of a star indicates a planet that crosses in front of the stellar disk. Owing to the observational biases of these techniques, the first planets thus discovered were the large, massive objects on few-day orbits commonly known as hot Jupiters (Mayor & Queloz 1995; Henry et al. 2000; Charbonneau et al. 2000). Their large sizes and high temperatures make these objects excellent candidates for the study of their dayside emission when the planet is occulted by the star (Deming et al. 2005; Charbonneau et al. 2005), of their longitudinally averaged global emission (Harrington et al. 2006; Cowan et al. 2007; Knutson et al. 2007), and of their atmospheric opacity via the wavelength-dependent flux diminution during transit (Seager & Sasselov 2000; Charbonneau et al. 2002). These observations have led to measurements of atmospheric abundances of key molecular species (Madhusudhan et al. 2011a), possible non-equilibrium chemistry (Stevenson et al. 2010), high-altitude hazes (Sing et al. 2009), and atmospheric circulation (Cowan & Agol 2011b).

Any discussion of hot-Jupiter atmospheres must necessarily mention two systems in particular. One, HD 189733, is the brightest star known to host a hot Jupiter (Bouchy et al. 2005). The other is HD 209458, the first known transiting planet (Charbonneau et al. 2000; Henry et al. 2000) and the focus of this study. These are the two touchstone objects in the study of irradiated giant exoplanets, both because they were discovered relatively early on and because they orbit especially bright (as seen from Earth) host stars. This last point in particular allows for especially precise characterization of these planets' atmospheres and permits observations which would provide unacceptably low signal-to-noise ratios (S/Ns) for fainter systems.

1.1. The HD 209458 System

The star HD 209458 is an F8 star roughly 15% more massive than the Sun (Mazeh et al. 2000; Brown et al. 2001; Baines et al. 2008), with an equivalent metallicity and slightly higher temperature (Schuler et al. 2011). It is orbited by HD 209458b,

[7] Alfred P. Sloan Research Fellow.
[8] CIERA Postdoctoral Fellow.

a roughly 1.4 R_J, 0.7 M_J planet in a 3.5 day, near-circular orbit (Southworth 2008; Torres et al. 2008). The planet's parameters have been substantially improved upon since its initial discovery (Charbonneau et al. 2000; Henry et al. 2000; Mazeh et al. 2000). Two sets of more recent values (Torres et al. 2008; Southworth 2008) do not differ significantly, and we use the former's system parameters in our analysis when not making our own measurements.

Infrared photometry during eclipses of HD 209458b measured from the ground (Richardson et al. 2003) and with *Spitzer* (Deming et al. 2005; Knutson et al. 2008) determines the planet's intrinsic emission spectrum, and is best fit by atmospheric models in which the planet's atmospheric temperature increases above ∼0.1–1 bar (Burrows et al. 2007, 2008; Fortney et al. 2008; Madhusudhan & Seager 2010). Such temperature inversions are common on hot Jupiters, and a popular explanation requires the presence of a high-altitude absorber (e.g., Fortney et al. 2008; Burrows et al. 2008). The nature of any such absorber is currently unknown and the subject remains a topic of active research (Désert et al. 2008; Spiegel et al. 2009; Knutson et al. 2010; Madhusudhan et al. 2011b).

If present, a high-altitude optical absorber is expected to absorb the incident stellar flux high in the atmosphere where radiative timescales are short and advection is inefficient (Cowan & Agol 2011a). Consequently, such planets are expected to exhibit large day/night temperature contrasts and low global energy redistribution despite circulation models' ubiquitous predictions of large-scale superrotating jets on these planets (Showman & Guillot 2002; Cooper & Showman 2005; Cho et al. 2008; Rauscher et al. 2008; Showman et al. 2009; Dobbs-Dixon et al. 2010; Burrows et al. 2010; Rauscher & Menou 2010; Thrastarson & Cho 2010; Heng et al. 2011a, 2011b). *Spitzer*/IRAC observations of HD 209458b at 8 μm place an upper limit on the planet's thermal phase variation of 0.0022 (3σ; Cowan et al. 2007). Given the planet's demonstrably low albedo (Rowe et al. 2008), this limit is substantially lower than expected if the planet has a low recirculation efficiency. In hot-Jupiter atmospheres, the dominant 24 μm molecular opacity source is expected to be H_2O, but there is some tension between models and past observations at this wavelength (see Madhusudhan & Seager 2010). Thus, our understanding of these planets' atmospheres remains incomplete.

Recent spectroscopic observations of HD 209458b during transit show a hint of a systematic velocity offset (2 ± 1 km s^{-1}) of planetary CO lines during planetary transit (Snellen et al. 2010). If confirmed, this offset would be diagnostic of high-altitude winds averaged over the planet's day/night terminator, and similar measurements at higher precision could one day hope to spatially resolve terminator circulation patterns and constrain atmospheric drag properties (Rauscher & Menou 2012). However, small orbital eccentricities (specifically, nonzero $e \cos \omega$, where ω is the longitude of periastron) can also induce a velocity offset in a planetary transmission spectrum (Montalto et al. 2011). It is thus convenient that precise timing of planetary transits and eclipses directly constrains $e \cos \omega$ (Seager 2011, chapter by J. Winn). This provides a further motivation for our work: to more tightly constrain HD 209458b's orbit via a homogeneous analysis of a single, comprehensive data set.

In this paper, we analyze the full complement of data for the HD 209458 system taken with the MIPS 24 μm camera (which we hereafter refer to simply as MIPS; Rieke et al. 2004) on the *Spitzer Space Telescope*. MIPS has taken previous 24 μm observations of exoplanetary transits (Richardson et al. 2006; Knutson et al. 2009a), eclipses (Deming et al. 2005; Charbonneau et al. 2008; Knutson et al. 2008, 2009b; Stevenson et al. 2010), and thermal phase curves (Harrington et al. 2006; Knutson et al. 2009b; Crossfield et al. 2010). MIPS operations depended on cryogenic temperatures; since *Spitzer*'s complement of cryogen has been exhausted, there may be no further exoplanet measurements at wavelengths of >10 μm until the eventual launch of missions such as *EChO*, *SPICA*, or the *James Webb Space Telescope* (*JWST*). Our work here describes some of the last unpublished 24 μm exoplanet observations, and a further motivation for our work is to inform the calibration, reduction, and observational methodologies of future missions' mid-infrared (MIR) observations.

Table 1
Spitzer/MIPS 24 μm Observations of HD 209458b

UT Date	Event	Duration (hr)	t_{int} (s)	$N_{exposures}$	Bkd[a] (MJy Sr^{-1})	Δt[b] (s)
UT 2004 Dec 5	Half-transit	2.8	8.91	840	28.8	−544
UT 2004 Dec 6	Eclipse	5.8	9.96	1680	29.2	−531
UT 2005 Jun 27	Transit	5.6	9.96	1680	28.9	−612
UT 2005 Dec 1	Eclipse	5.6	9.96	1680	26.7	+183
UT 2008 Jul 25[c]	Transit[d]	14.2	9.96	4060	28.3	−649
UT 2008 Jul 27[c]	Eclipse	6.9	9.96	2072	27.9	−663

Notes.
[a] Average sky backgrounds as reported by DRIBKGND keyword.
[b] For each event, $\Delta t \equiv \langle \mathrm{HJD} \rangle - \langle \mathrm{BJD_{TDB}} \rangle$.
[c] These events were observed as part of a single, continuous phase curve observation with a duration of 58 hr spanning one transit and one secondary eclipses.
[d] This transit was corrupted by an apparent ramp in detector sensitivity, so we used a longer section of data to better constrain the ramp parameters in the joint fit.

1.2. Outline

This report is organized as follows: in Section 2, we describe the MIPS observations and our approach to measuring precise system photometry. In Section 3, we describe our efforts to understand the origin of instrumental sensitivity variations apparent in the long-duration phase curve observations; these effects ultimately prevent any measurement of HD 209458b's thermal phase curve. However, we are able to recover the parameters of the observed transits and eclipses, and we present these results in Sections 4 and 5, respectively. Combining the results of these two analyses allows us to constrain the planet's orbit (i.e., $e \cos \omega$), and we discuss the implications of this, and of the total system flux in Section 6. We summarize our conclusions and present some thoughts for future high-precision MIR observations in Section 7.

2. OBSERVATIONS AND ANALYSIS

2.1. Observations

We reanalyzed all observations of the HD 209458 system taken with *Spitzer*'s MIPS 24 μm channel: analysis of one transit, two eclipses, and the long-duration phase curve observations have remained unpublished until now. Altogether, we used the data from Spitzer Program IDs 3405 (PI: Seager; published in Deming et al. 2005), 20605 (PI: Harrington; published in Richardson et al. 2006), and 40280 (PI: Knutson). Table 1 lists the observatory parameters used for each set of observations.

Collectively, these data comprise two and a half transits, three eclipses, and a 58 hr set of near-continuous observations designed to detect the planet's thermal phase curve.

2.2. Data Reduction

Unless stated otherwise, we use the same methodology to reduce our data as described in Crossfield et al. (2010, hereafter C10), performing PSF-fitting photometry using a 100× supersampled MIPS PSF[9] modeled using a 6070 K blackbody spectrum simulated at the center of the MIPS field of view. We vary the size of the synthetic aperture used to calculate our PSF-fitting photometry, and find that a square, 21×21 pixel aperture minimizes photometric variations. During MIPS observations, the target star is dithered between 14 positions on the detector (Colbert 2011, Section 8.2.1.2), and we fit the data from all dither positions simultaneously as described below.

As noted by C10, the MIPS 24 μm detector appears to suffer from low-amplitude temporal variations in the diffuse background, presumably owing to small amounts of scattered light in the instrument. Because this could affect the flat fielding performed by the MIPS reduction pipeline, we create an empirical flat field by taking a pixel-by-pixel median of all the individual frames after masking the region containing the target star. After constructing this flat field, we extract photometry (1) after subtracting the master flat field from each frame, and (2) after dividing each frame by the normalized-to-unity master flat field. Both of these give photometry that is very slightly less noisy (rms reduced by $\lesssim$1%) than photometry that does not use an additional flat-field correction. Subtracting by the empirical flat field prior to computing PSF-fitting photometry results in a lower residual rms and so we use this approach for all our data; ultimately, our choice of flat field does not change our final results.

We extract the Heliocentric Julian Date (HJD) from the timing tags in each BCD data file, and then convert the HJD values to $\mathrm{BJD_{TDB}}$ using the IDL routine `hjd2bjd`[10] (Eastman et al. 2010). These new time stamps have an estimated accuracy of one second (Eastman et al. 2010), which is small compared to our final ephemeris uncertainties of roughly one and four minutes for transits and eclipses, respectively.

2.3. Approach to Model Fitting

The MIPS dither pattern introduces systematic offsets of $\lesssim$1% (Deming et al. 2005) in the photometry at each dither position. We follow the methodology of C10 and explicitly fit for this effect by multiplying the modeled flux for each visit at dither position i by the factor $(1+c_i)$. We further impose the constraint that these corrections do not change the absolute flux level, and so define c_0 such that the quantity $\prod_i (1+c_i)$ is equal to unity. We ultimately find that the c_i are similar, but not constant, from one epoch to the next.

In all cases, we determine best-fit model parameters using the Python simplex minimization routine `scipy.optimize.fmin`.[11] We assess parameter uncertainties using a Markov Chain Monte Carlo (MCMC) implementation of the Metropolis–Hastings algorithm (`analysis.generic_mcmc`[12]), then take as uncertainties the range of values (centered on the best-fit value) that enclose 68.3% of the posterior distribution. We verify by eye that the Markov chains are well mixed; the resulting one-dimensional posterior distributions are unimodal, symmetric, and approximately Gaussian unless stated otherwise.

[9] Generated using Tiny Tim; available at http://ssc.spitzer.caltech.edu/
[10] Available at http://astroutils.astronomy.ohio-state.edu/time/
[11] Available at http://scipy.org/
[12] Currently available at http://www.astro.ucla.edu/~ianc/python/

3. CALIBRATION AND INSTRUMENT STABILITY

3.1. The Ramp

Before we present the results of our model fits, we discuss two photometric variations that we conclude to be of instrumental origin. The HD 209458 system flux measured from our 2008 observations, shown in Figure 1, exhibits a steep rise during the first 10–12 hr in which the measured system flux increases by ∼2%. This ramp appears similar to that seen in photometric observations taken with *Spitzer*/IRAC and *Spitzer*/IRS (Charbonneau et al. 2005; Deming et al. 2006; Knutson et al. 2007). The IRAC ramp is the better studied, and is thought to result from charge trapping in the detector (see Knutson et al. 2007; Agol et al. 2010). According to this explanation, a substantial fraction of photoelectrons liberated early in the observations become trapped by detector impurities, resulting in a lower effective gain for the detector. Eventually, all charge-trapping sites become populated and the detector response asymptotes to a constant level. As the IRAC 8 μm, IRS 16 μm, and MIPS detectors are all constructed of Si:As, it is conceivable that the MIPS ramp we observe has a similar origin in charge trapping.

To test this hypothesis, we look for evidence of persistence in our data. Using all frames taken at the second dither position, we compute the median image from each of several Astronomical Observing Requests (AORs). An AOR is a *Spitzer* logistical unit comprising some dozens of frames; in our data set each AOR lasts approximately three hours. We see faint afterimages at the other 13 dither positions when we subtract the first median AOR frame from the final median AOR frame (taken ∼56 hr later; see Figure 1), which suggests that the level of persistence (a byproduct of charge trapping) increases over the course of the observations. These afterimages are much fainter when comparing data from the first and second AORs (separated by 3.6 hr), consistent with the conclusion that the level of persistence does not saturate to a constant value on these short timescales. The afterimages are not apparent by eye when comparing the last and penultimate AORs (again separated by 3.6 hr), which suggests that the charge-trapping persistence has saturated by this time, as expected from the much-flattened data ramp seen in Figure 1.

The IRAC ramp is known to exhibit a behavior which depends on the level of illumination, with more intensely illuminated pixels exhibiting a steeper initial ramp and saturating more quickly (these pixels' charge traps are filled more quickly because more free photoelectrons are available). We see a hint of this behavior in our data. Though pointing variations prevent us from tracking the response of individual pixels, we extract photometry (again via PSF fitting) using both 3- and 5-pixel-wide square apertures. The 3-pixel photometry—which is weighted somewhat more heavily by the most intensely illuminated pixels than is the 5-pixel photometry—shows a hint of a steeper ramp. We take this as further tentative support for our hypothesis that our ramp has a common origin with the IRAC ramp. The ramp behavior remains unchanged when we use a wider aperture, but this may not be diagnostic since the gradient in illumination level quickly flattens out beyond a few pixels.

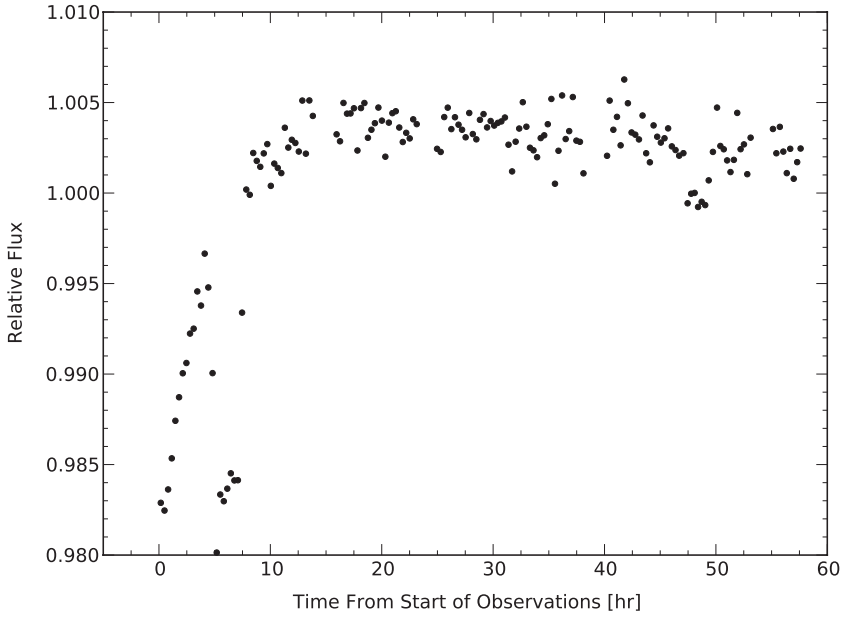

Figure 1. MIPS 24 μm photometry of the HD 209458 system, showing the detector ramp (0–10 hr), transit (5 hr), and eclipse (48 hr). For plotting purposes, the data have been binned to lower temporal resolution. A slight ($\sim$0.2%) flux decrease is apparent from 10 to 58 hr. This could be influenced by planetary phase variations, but the similarity to the purely instrumental effects seen in Figure 2 precludes an unambiguous distinction between the two effects.

We would like to know why we see this ramp, especially considering that no previous MIPS observations detected this effect. However, we can find no consistent discriminant between the presence or absence of a ramp in MIPS data and the state of either instrument or observatory. The first set of AORs in C10's observations (the first $\sim$10 hr) were anomalously low ($\sim$0.3%) compared to subsequent observations, which they attributed to a thermal anneal of the 24 μm detector conducted $<$1 hr before these observations.[13] No ramp was observed in the continuous, long-duration MIPS observations of either Knutson et al. (2009b) or C10, which were taken $\gtrsim$1 day after the last 24 μm anneal. The photometry shown in Figure 1 also occurred $>$1 day after the last 24 μm anneal, so annealing seems unlikely to explain the presence of the ramp in our data.

We investigated whether pre-flashing could explain the absence of any ramp in other MIPS phase curve observations. To pre-flash is to conduct a set of brief ($<$1 hr) observations of a bright target before observing a fainter exoplanet system (Seager & Deming 2009; Knutson et al. 2011); experience shows that this tends to reduce the amplitude of the ramp, presumably by partially saturating the detector's charge traps. HD 209458 is the faintest of the three exoplanet systems with long-duration MIPS 24 μm observations, but the flux difference ($\sim$20 mJy for HD 209458 versus $\sim$60 mJy for HD 189733) does not seem sufficiently large for only one of our five observations of HD 209458 to fail to pre-flash the detector. If the difference were due to the increased flux from HD 189733, then we should still see a shorter, steeper ramp at the start of these observations. That no ramp has been reported previously, and that we see a ramp in the HD 209458 data only intermittently, suggests that some other phenomenon may be at work here.

The phase curve observations of both HD 189733 and HD 209458 began immediately after a data downlink to Earth, so this factor also does not distinguish between the cases. Prior to the data downlinks, our 2008 observations of HD 209458 were preceded by 24 μm observations of the faint RXCJ0145.2-6033 ($\sim$4 mJy), but no 24 μm observations whatsoever were made in the $\sim$day leading up to Knutson et al.'s (2009b) observations of HD 189733. While MIPS was operational, all its arrays were continuously exposed to the sky: although the *Spitzer* operations staff planned observations so as to avoid placing bright sources on the 24 μm array (using *IRAS* 25 μm images as a guide; A. Noriega-Crespo 2011, private communication), we cannot dismiss the possibility that occasionally some bright sources may have been missed.

Thus, we cannot conclusively determine why the MIPS observations of HD 209458 we present here show the detector ramp while previous, comparable observations have not shown such an effect. Nonetheless, the similarity between our photometry in Figure 1 and raw IRAC 8 μm photometry (e.g., Agol et al. 2010) strongly suggests that the most likely explanation involves detector response variations due to charge trapping.

3.2. The Fallback

After the detector ramp, the photometry in Figure 1 decreases over the rest of the observations by $\sim$0.2%; we term this flux diminution the "fallback." The amplitude of this effect is of the approximate amplitude expected for a 24 μm planetary thermal phase curve (Showman et al. 2009; Burrows et al. 2010), so our first inclination was to ascribe a planetary origin to this flux decrease. However, there is a distinct qualitative similarity between the phase curve photometry and pre-launch calibration data taken with the MIPS 24 μm detector under bright (170 MJy sr^{-1}) illumination, shown in Figure 2 (reproduced from Young et al. 2003). A comparison of this figure and Figure 1 reveals that both display the same qualitative signature of an early, steep ramp followed by a slow, gradual fallback in measured flux. The only differences are (1) an initial steep decrease in flux in the calibration data not seen in our stellar photometry (attributed by Young et al. 2003, to the response of the detector to a thermal

[13] As recorded in the *Spitzer* observing logs, available at http://ssc.spitzer.caltech.edu/warmmission/scheduling/observinglogs/

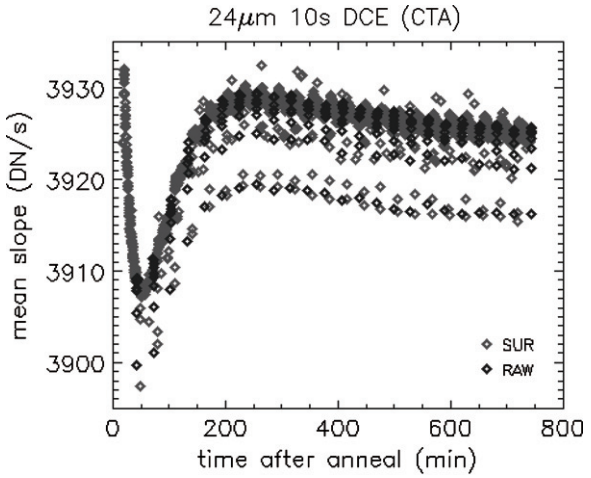

Figure 2. Lab calibration data for the MIPS 24 μm array, taken from Young et al. (2003, their Figure 7). The relevant data for comparison with *Spitzer*/MIPS observations are the gray diamonds labeled SUR (Sample Up the Ramp, the algorithm used to compute MIPS data numbers from pixel slopes). Young et al. (2003) suggest that the initial sensitivity decrease (0–50 minutes) is related to detector response variations related to a thermal anneal immediately preceding the data; as we describe in Section 3, our data should not be affected by any anneal operations. The rest of the observations appear strikingly similar to our photometry of HD 209458, shown in Figure 1. For comparison with Figure 1, the peak pixel fluxes in the HD 209458 data frames are roughly 1000 DN s^{-1}.

anneal immediately preceding the data shown), and (2) longer ramp and fallback time constants in our data set.

The brightest pixels in the HD 209458 MIPS observations reach a flux of 45 MJy sr^{-1} (corresponding to 1000 DN s^{-1}). Perhaps, like in some pre-flashed IRAC observations (see Knutson et al. 2011), the lower illumination level in the HD 209458 photometry (relative to the stimulation response curve from Young et al. 2003) is responsible for the different timescales evident in the two 24 μm time series. However, the brightest pixels in the observations of C10 reached a flux of 9000 DN s^{-1} and no fallback is apparent in the continuous portion of those observations (though C10's continuous photometry did decrease monotonically by ~0.1%, they demonstrated a coherent planetary phase curve in two data sets spanning several years; thus, planetary emission, rather than an instrumental sensitivity variation, seems a more likely interpretation of their results). Similarly, no fallback is seen in MIPS observations of HD 189733b (peak pixel flux ~1200 DN s^{-1}; Knutson et al. 2009b) or of the fainter eclipsing M binary GU Boo ($\lesssim$500 DN s^{-1}; von Braun et al. 2008). Thus, it seems possible that the fallback is linked to the presence of the detector ramp, which also appears only in our MIPS data set.

We try a number of different functional forms to fit to the ~0.2% post-ramp fallback, which we fit simultaneously with the ramp. These include a flat model (i.e., no decrease), sinusoidal and Lambertian profiles with arbitrary amplitude and phase (representative of a planetary phase curve), and a double-exponential of the form $(1 - \alpha e^{-t/\tau_1}) \times e^{-t/\tau_2}$, with $\tau_2 \gg \tau_1$, motivated by the detector response variations seen in Figure 2. We decide which of these models is the most appropriate on the basis of the Bayesian information criterion (BIC[14]). The model consisting of a ramp plus a decaying exponential gives the lowest BIC: ~15 units lower than obtained with the sinusoidal or Lambertian models. Thus, the data prefer an instrumental explanation for the low-level flux variations that we see.

When using a sinusoidal or Lambertian model, the best-fit phase curve parameters describe a thermal phase variation which peaks well before secondary eclipse, suggesting a planetary hot spot eastward of the substellar point. Qualitatively, such a shift is consistent with observations of both HD 189733b (Knutson et al. 2009b) and υ and b (C10). However, the phase offset determined by this fitting process is surprisingly large: 136° ± 18°, a result which would seem to imply that the planet's night side is hotter than its day side. Such a scenario has been predicted by some models (see Cho et al. 2003), but such a large phase offset is bigger than observed for either υ and b or HD 189733b, and larger still when compared to expectations for this planet from more recent simulations (e.g., Rauscher et al. 2008; Showman et al. 2009). We thus deem the phase curve fit with large offset to be an unlikely result, providing one more reason to doubt that the flux variation we see is of planetary origin.

We also inject into the data a sinusoidal phase curve with zero phase offset and a peak-to-valley amplitude equal to our best-fit secondary eclipse depth results and repeat our analysis: in this case the best-fit sinusoidal and Lambertian models have a lower BIC value (by 12 units) than the instrumental model, though the recovered amplitude and phase offset are still somewhat biased by the flux fallback. Although these results suggest that we are close to achieving the sensitivity required to constrain HD 209458b's thermal phase variations, our ignorance of the detailed morphology of the flux fallback prevents us from reaching a more quantitative conclusion. Thus, we can only conclude that the striking qualitative similarity between Figures 1 and 2 precludes us from making any definite claims as to the detection of planetary phase curve effects in our data.

3.3. Instrument Stability

As observed previously by C10, the background flux of continuous MIPS photometry exhibits a roughly linear trend with time, with smaller, abrupt changes from one AOR to the next. The linear trend can be explained by a variation in the thermal zodiacal light as *Spitzer*'s perspective of HD 209458 changes with respect to the solar system, and C10 attribute the discontinuous, AOR-by-AOR background fluctuations to scattered light. Whatever the cause, these discontinuities are removed by the sky background subtraction, and do not appear to affect the final stellar photometry.

During our 2008 observations, we see a 0.5 μA increase in the 24 μm detector anneal current (MIPS data file keyword AD24ANLI), a decrease of 6 mK in the scan mirror temperature (keyword ACSMMTMP), and swings in the electronics box temperature (keyword ACEBOXTM) of up to 0.3 K. During sustained observations, the electronics box appears to experience heating with some time lag, but with a much shorter cooling lag during observational breaks to transmit data to Earth. Upon reexamination of past observations, we find that these three parameters exhibit similar behavior during observations of HD 189733b (Knutson et al. 2009a) and of upsilon Andromeda b (C10). The MIPS optical train is cryogenically cooled and separated from the non-cryogenic instrument electronics (Heim et al. 1998), so it does not seem likely that the observed swings in the electronics box temperature should influence the photometry. Similarly, the anneal current and scan mirror temperature do not seem to correlate with either the ramp or the post-ramp flux decrease, so

[14] BIC = $\chi^2 + k \ln N$, where k is the number of parameters to be fit and N the number of data points. A fit that gives a lower BIC is preferred over a fit with a higher BIC, and thus the BIC penalizes more complicated models.

Table 2
Joint Transit Fits

Parameter	2004	2005	2008
c_0	$+0.0009 \pm 0.0022$	$+0.00036 \pm 0.00086$	$+0.00274 \pm 0.00053$
c_1	$+0.0097 \pm 0.0027$	$+0.00881 \pm 0.00088$	$+0.01387 \pm 0.00055$
c_2	-0.0030 ± 0.0022	$+0.00101 \pm 0.00136$	$+0.00487 \pm 0.00053$
c_3	$+0.0106 \pm 0.0024$	$+0.00866 \pm 0.00079$	$+0.00858 \pm 0.00056$
c_4	-0.0034 ± 0.0024	$+0.00148 \pm 0.00115$	-0.00020 ± 0.00053
c_5	-0.0021 ± 0.0032	$+0.01006 \pm 0.00080$	$+0.01310 \pm 0.00052$
c_6	$+0.0017 \pm 0.0022$	-0.00574 ± 0.00078	-0.00502 ± 0.00057
c_7	-0.0023 ± 0.0033	$+0.00167 \pm 0.00081$	-0.00720 ± 0.00054
c_8	-0.0036 ± 0.0023	-0.00298 ± 0.00078	-0.00121 ± 0.00058
c_9	$+0.0098 \pm 0.0023$	-0.00324 ± 0.00135	-0.00919 ± 0.00060
c_{10}	-0.0032 ± 0.0028	$+0.00394 \pm 0.00111$	$+0.00210 \pm 0.00057$
c_{11}	-0.0126 ± 0.0032	-0.00974 ± 0.00103	-0.01016 ± 0.00057
c_{12}	$+0.0008 \pm 0.0028$	-0.00039 ± 0.00085	-0.00122 ± 0.00065
c_{13}	-0.0028 ± 0.0024	-0.01360 ± 0.00091	-0.01062 ± 0.00052
F_* (mJy)	$+18.845 \pm 0.012$	$+18.7784 \pm 0.0049$	$+18.696 \pm 0.010$
α	...	...	$+0.02437 \pm 0.00068$
τ (day)	...	...	$+0.174 \pm 0.016$
$T_{c,t}$ ($\mathrm{BJD_{TDB}}$)		$2453549.20852 \pm 0.00049$	
b		$+0.590 \pm 0.062$	
R_*/a		$+0.1205 \pm 0.0066$	
R_p/R_*		$+0.1218 \pm 0.0014$	
$(R_p/R_*)^2$ [a]		$+0.01483 \pm 0.00033$	

Note. [a] Computed from the posterior MCMC distributions of R_P/R_*.

we conclude that these instrumental variations do not affect our final photometry.

4. TRANSITS

4.1. Fitting Approach

We fit transits using uniform-disk and linear limb-darkened transit models (Mandel & Agol 2002), but (consistent with the results of Richardson et al. 2006) we find the limb-darkened model offers no improvement over the uniform-disk model (as determined by the BIC). We fit the transit data for: the time of center transit $T_{c,t}$, the impact parameter b, the scaled stellar radius R_*/a, the planet/star radius ratio R_p/R_*, and the out-of-transit system flux F_*. We hold the period fixed at $3.52474550 \pm 0.00000018$ days (Torres et al. 2008), which is a more precise determination than our observations can provide. To extract useful information from our half-transit event we always require that b and R_*/a have the same value, determined jointly from all our transits. We therefore perform one fit in which these two parameters are jointly fit, and a second fit in which we additionally fit jointly to $T_{c,t}$ and R_p/R_* across all transit events.

We fit to the detector ramp in the 2008 transit by including a multiplicative factor of the form $1-\alpha e^{-t/\tau}$, where t is measured from the start of the observations. This formulation of the ramp model is motivated by a physical model of the charge-trapping phenomenon thought to cause the IRAC 8 μm ramp (Agol et al. 2010). Agol et al. (2010) find a ramp based on two exponentials to be preferred for their high S/N observations, but we find that our data are not precise enough to constrain this more complicated model: when fitting a double-exponential ramp of the form $1 - \alpha_1 e^{-t/\tau_1} - \alpha_2 e^{-t/\tau_2}$ (Agol et al. 2010), the parameters for the two exponential trends become degenerate, and the resulting fits are not preferred to the single ramp fit on the basis of the BIC. Finally, we include in all our fits the 14 sensitivity correction terms (c_i) corresponding to the 14 MIPS dither positions.

4.2. Results

Table 2 lists the results of the fit in which we assume a constant orbit and transit—holding b, R_*/a, R_p/R_*, and $T_{c,t}$ constant across all transits—while Table 3 lists the results of the fit in which R_p/R_* and $T_{c,t}$ (but not b or R_*/a) are allowed to vary between events. We plot the results of fits to each individual transit, and to the combined data set, in Figure 3. We show how the residuals to the combined fit bin down with increasing sample size in Figure 4: the curve shown tracks closely with the $N^{-1/2}$ expectation from uncorrelated noise on short timescales (<20 minutes), but on longer timescales the residuals bin down more slowly than this. This indicates the presence of correlated (red) noise (see Pont et al. 2006) in these data, which is not surprising considering the ramp residuals apparent in Figure 3.

We examine the residuals to the 14 individual channels and see some evidence for qualitatively different correlated noise at different dither positions. We do not think it likely that this behavior is related to an intrapixel effect (as observed in IRAC; see Charbonneau et al. 2005) because the residual behavior we see does not correlate with mean PSF position relative to the boundaries of individual pixels. Instead, it seems more likely to be a manifestation of the known position-dependent sensitivity effect previously attributed to residual flat-fielding errors (Crossfield et al. 2010).

The resulting posterior distributions are all unimodal (except for the impact parameter b), and the usual correlations are apparent between b and R_*/a and between F_* and R_p/R_* (see Burke et al. 2007). As noted above, the 2008 transit data are strongly affected by the detector ramp, and we see correlations between the ramp parameters and the transit depth. We compute the two-dimensional posterior distributions of R_P/R_*, τ, and α (marginalized over all other parameters) from the MCMC chains using the kernel density estimate approach described in C10; we show these distributions in Figure 5 and list the elements of these parameters' covariance matrix in Table 4.

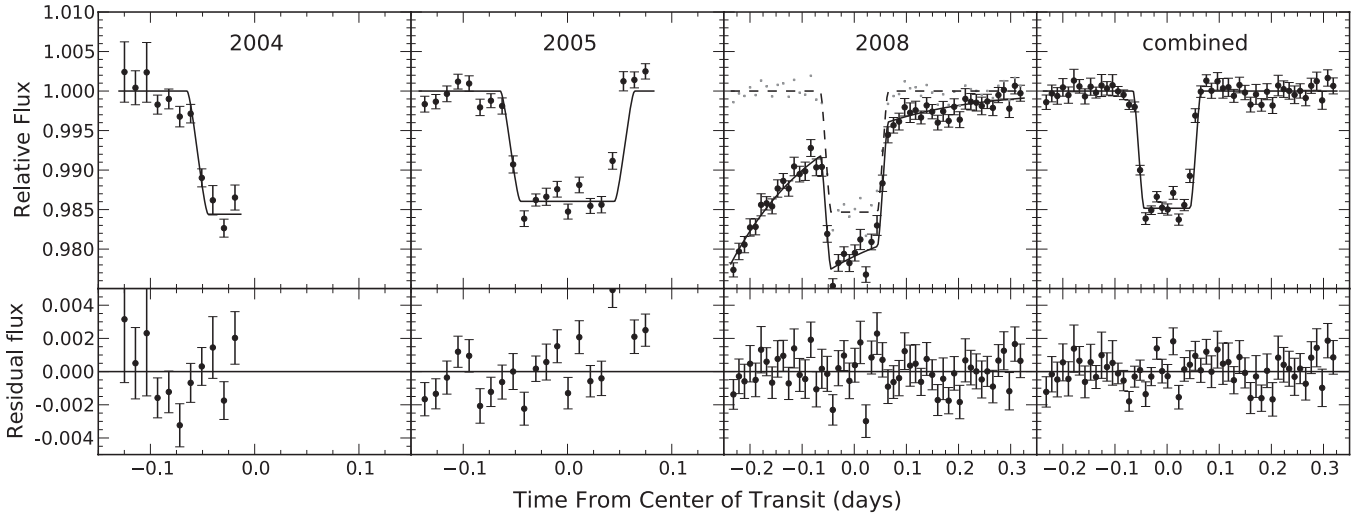

Figure 3. MIPS 24 μm transits of HD 209458b. The top panels show photometry and the best-fit model, and the lower panels show the residuals to the fits. For plotting purposes, the data have been corrected for the MIPS 14-position sensitivity variations, normalized by the stellar flux, and binned by 70 points (for the individual transits) and by 210 points (for the combined data set). We also corrected for the ramp in the 2008 data set (corrected, binned data shown as small points) before combining the data to plot the data in the rightmost panel.

Table 3
Semi-joint Transit Fits

Parameter	2004	2005	2008
c_0	-0.0001 ± 0.0024	$+0.00043 \pm 0.00084$	$+0.00268 \pm 0.00054$
c_1	$+0.0091 \pm 0.0030$	$+0.00866 \pm 0.00095$	$+0.01368 \pm 0.00053$
c_2	-0.0032 ± 0.0022	$+0.00087 \pm 0.00149$	$+0.00524 \pm 0.00076$
c_3	$+0.0117 \pm 0.0023$	$+0.00872 \pm 0.00082$	$+0.00878 \pm 0.00066$
c_4	-0.0032 ± 0.0023	$+0.00146 \pm 0.00110$	-0.00016 ± 0.00053
c_5	-0.0021 ± 0.0029	$+0.01009 \pm 0.00078$	$+0.01316 \pm 0.00053$
c_6	$+0.0019 \pm 0.0022$	-0.00603 ± 0.00084	-0.00516 ± 0.00053
c_7	-0.0019 ± 0.0039	$+0.00157 \pm 0.00083$	-0.00686 ± 0.00058
c_8	-0.0039 ± 0.0023	-0.00301 ± 0.00078	-0.00110 ± 0.00063
c_9	$+0.0095 \pm 0.0022$	-0.00317 ± 0.00144	-0.00910 ± 0.00057
c_{10}	-0.0032 ± 0.0029	$+0.00378 \pm 0.00093$	$+0.00189 \pm 0.00052$
c_{11}	-0.0124 ± 0.0028	-0.00942 ± 0.00082	-0.00977 ± 0.00056
c_{12}	$+0.0007 \pm 0.0028$	-0.00035 ± 0.00086	-0.00189 ± 0.00129
c_{13}	-0.0026 ± 0.0022	-0.01330 ± 0.00078	-0.01096 ± 0.00061
$T_{c,t}$ (BJD$_{\rm TDB}$)	2453344.7718 ± 0.0025	$2453549.20746 \pm 0.00065$	$2454673.60391 \pm 0.00074$
R_p/R_*	$+0.1227 \pm 0.0060$	$+0.1189 \pm 0.0020$	$+0.1238 \pm 0.0019$
F_* (mJy)	$+18.850 \pm 0.016$	$+18.7735 \pm 0.0056$	$+18.6947 \pm 0.0095$
$(R_p/R_*)^2$ [a]	$+0.0151 \pm 0.0015$	$+0.01413 \pm 0.00046$	$+0.01531 \pm 0.00046$
α	...	...	$+0.02458 \pm 0.00071$
τ (day)	...	...	$+0.168 \pm 0.016$
b		$+0.581 \pm 0.070$	
R_*/a		$+0.1197 \pm 0.0069$	

Note. [a] Computed from the posterior MCMC distributions of R_P/R_*.

Table 4
Ramp and Transit Depth Covariance Matrix (see Figure 5)

Element	Value/10^6
σ^2_α	0.507
$\sigma^2_{\tau[d]}$	266 day^2
$\sigma^2_{R_p/R_*}$	3.49
$\sigma_{\alpha,\tau[d]}$	-5.03 days
$\sigma_{\alpha,R_p/R_*}$	0.379
$\sigma_{\tau[d],R_p/R_*}$	-16.3 days

4.3. Discussion

The three independently fit transit depths listed in Table 3 have a fractional dispersion of 3%, consistent with our individual uncertainty estimates of 3%–10%. We thus find no evidence for variations in transit depth, and our transit depths are consistent with the depth measured from the combination of our first two transit data sets (Richardson et al. 2006).

We plot the ensemble of HD 209458b's transit depth measurements in Figure 6 along with a model of transit depth versus wavelength from Fortney et al. (2010). The model is consistent with the 24 μm measurement we present here and agrees fairly well with the optical measurements of Sing et al. (2008) and the IRAC 3.6 and 4.5 μm measurements of Beaulieu et al. (2010). However, our model strongly disagrees with the IRAC 5.8 and 8.0 μm, which was also shown for the same HD 209458b model in Fortney et al. (2010). The large discrepancy remains unclear. Given the known wavelength-dependent water vapor

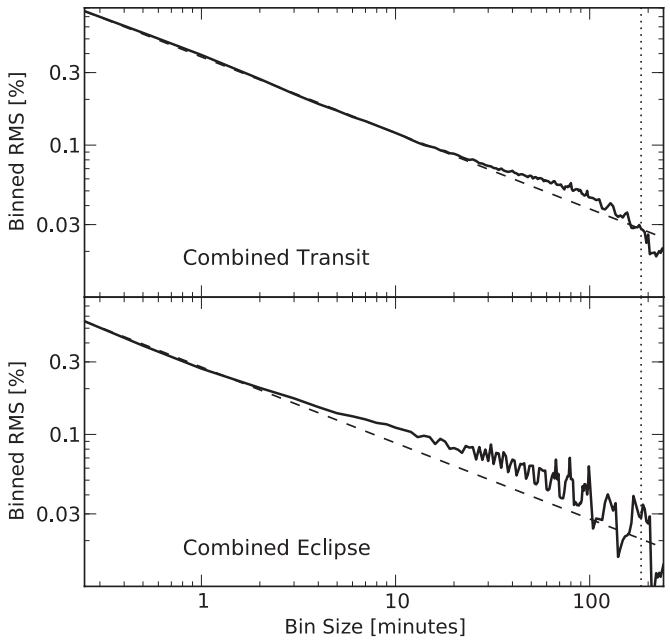

Figure 4. Dispersion of the binned residuals (solid lines) to the combined transit and eclipse light curve fits shown in Figures 3 and 7. On longer timescales, both fits exhibit a binned dispersion 10%–30% higher than expected from uncorrelated noise (dashed line). The dashed lines show the expectation for uncorrelated errors, which scale as $N^{-1/2}$. The vertical dotted line indicates the transit duration.

opacity, Shabram et al. (2011) showed that reaching all four IRAC data points may be impossible within the framework of a simple transmission spectrum model. Our transmission spectrum methods are described in these papers, and the atmospheric pressure–temperature profile is from a planet-wide average no-inversion model shown in Figure 9.

We resample the posterior distributions of the independent transit ephemerides shown in Table 3 to determine our own, independent constraint on the planet's orbital period (assuming it is constant) using a linear relation. We compute the center-of-transit time and period to be 2453549.2075 ± 0.0013 days and 3.5247537 ± 0.0000049 days, respectively; the covariance between these two parameters is -5.652×10^{-9} day^2. The period we obtain differs from the established period (Torres et al. 2008) by only 8.2×10^{-6} days (0.71 s), well within the uncertainties.

5. SECONDARY ECLIPSES

5.1. Fitting Approach

We fit secondary eclipses using the uniform-disk occultation formulae of Mandel & Agol (2002), fitting each event for three astrophysical parameters: time of center of eclipse $T_{c,e}$, stellar flux F_*, and eclipse depth F_p/F_*—as well as the 14 sensitivity correction terms (c_i) discussed previously. We hold all other orbital parameters fixed at the values listed in Torres et al. (2008), which are more precise than our constraints based on the 24 μm transit photometry. We perform four different fits: an independent fit of each eclipse taken in isolation, and a fit to the combined data set in which we fit for a single eclipse depth, but still allow $T_{c,e}$ and F_* to vary for each event. We use only a subset of the long-duration phase curve observations to fit the 2008 eclipse, as indicated in Table 1. We tried including a linear slope in the combined eclipse fit, but this extra parameter is not justified because it gives a higher BIC than fits without such a slope.

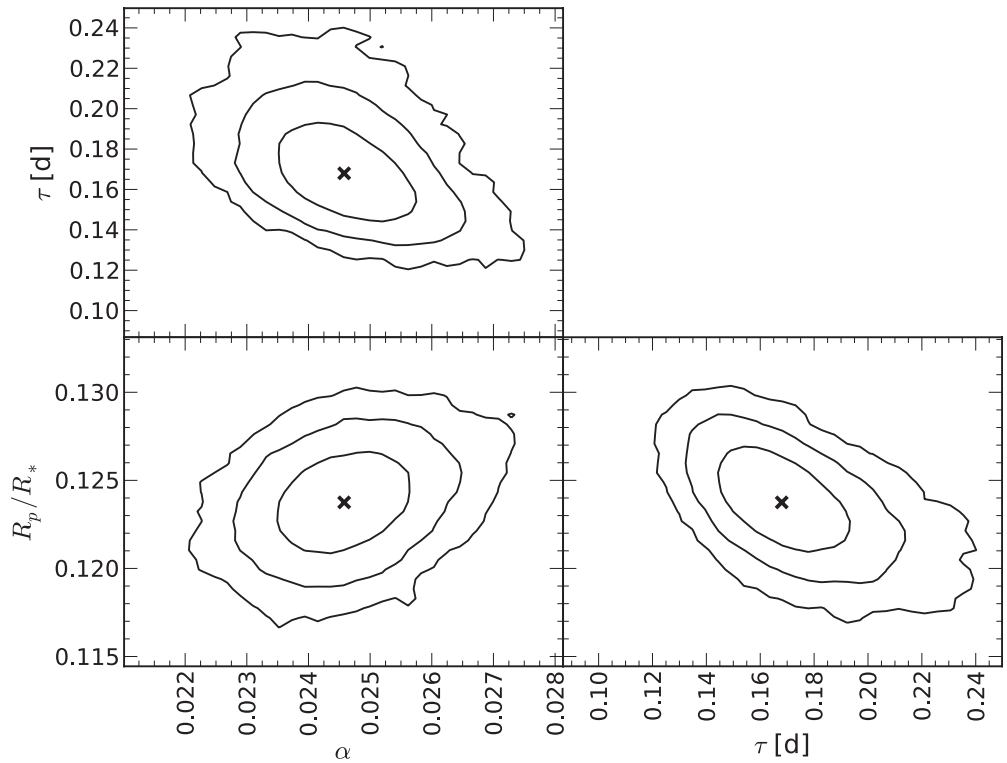

Figure 5. Posterior distributions of the ramp parameters (α, τ) and R_p/R_*, estimated from the MCMC analysis of the 2008 transit data. The "×" symbols indicate the best-fit parameters listed in Table 3, and the lines indicate the 68.27%, 95.45%, and 99.73% confidence intervals. The elements of these parameters' covariance matrix are listed in Table 4.

Table 5
Joint Eclipse Fits

Parameter	2004	2005	2008
c_0	+0.00298 ± 0.00080	+0.00048 ± 0.00078	+0.00278 ± 0.00073
c_1	+0.00793 ± 0.00078	+0.01103 ± 0.00080	+0.01331 ± 0.00071
c_2	+0.00619 ± 0.00079	+0.00349 ± 0.00078	+0.00397 ± 0.00074
c_3	+0.00943 ± 0.00075	+0.00879 ± 0.00078	+0.00887 ± 0.00071
c_4	+0.00048 ± 0.00108	+0.00186 ± 0.00102	−0.00002 ± 0.00074
c_5	+0.01148 ± 0.00080	+0.01151 ± 0.00079	+0.01480 ± 0.00069
c_6	−0.00557 ± 0.00079	−0.00461 ± 0.00084	−0.00432 ± 0.00072
c_7	−0.00571 ± 0.00082	−0.00582 ± 0.00079	−0.00514 ± 0.00072
c_8	−0.00171 ± 0.00078	−0.00020 ± 0.00082	−0.00329 ± 0.00070
c_9	−0.00231 ± 0.00079	−0.00361 ± 0.00079	−0.00754 ± 0.00070
c_{10}	+0.00052 ± 0.00082	+0.00084 ± 0.00093	−0.00137 ± 0.00080
c_{11}	−0.00691 ± 0.00081	−0.00973 ± 0.00076	−0.00712 ± 0.00073
c_{12}	−0.00507 ± 0.00082	−0.00402 ± 0.00078	−0.00333 ± 0.00072
c_{13}	−0.01142 ± 0.00079	−0.00968 ± 0.00081	−0.01121 ± 0.00071
F_* (mJy)	+18.78683 ± 0.00486	+18.70529 ± 0.00485	+18.60906 ± 0.00472
	F_p/F_*	+0.00338 ± 0.00026	
	T_B (K)	+1310 ± 80	
	F_p (μJy)[a]	+63.2 ± 4.9	
	$T_{c,e}$ (BJD_{TDB})[b]	2453706.0595 ± 0.0014	

Notes.
[a] Computed from the posterior MCMC distributions of F_* and F_p/F_*.
[b] Jointly fit ephemeris, assuming a period of 3.5247455 days (Torres et al. 2008).

Table 6
Independent Eclipse Fits

Parameter	2004	2005	2008
c_0	0.00262 ± 0.00090	−0.00020 ± 0.00112	0.00044 ± 0.00264
c_1	0.00744 ± 0.00089	0.01028 ± 0.00124	0.01246 ± 0.00114
c_2	0.00500 ± 0.00169	0.00396 ± 0.00084	0.00449 ± 0.00106
c_3	0.00879 ± 0.00101	0.00879 ± 0.00077	0.00850 ± 0.00075
c_4	−0.00042 ± 0.00090	0.00198 ± 0.00111	0.00143 ± 0.00160
c_5	0.01090 ± 0.00104	0.01109 ± 0.00091	0.01392 ± 0.00115
c_6	−0.00488 ± 0.00106	−0.00502 ± 0.00109	−0.00351 ± 0.00120
c_7	−0.00453 ± 0.00138	−0.00331 ± 0.00284	−0.00561 ± 0.00086
c_8	−0.00248 ± 0.00109	−0.00078 ± 0.00089	−0.00249 ± 0.00105
c_9	−0.00230 ± 0.00082	−0.00239 ± 0.00142	−0.00744 ± 0.00073
c_{10}	0.00113 ± 0.00118	0.00086 ± 0.00093	0.00079 ± 0.00225
c_{11}	−0.00588 ± 0.00118	−0.01021 ± 0.00097	−0.01012 ± 0.00328
c_{12}	−0.00315 ± 0.00201	−0.00385 ± 0.00078	−0.00189 ± 0.00171
c_{13}	−0.01197 ± 0.00104	−0.01090 ± 0.00166	−0.01059 ± 0.00098
$T_{c,e}$ (BJD_{TDB})[a]	2453346.5348 ± 0.0028	2453706.0600 ± 0.0029	2454675.3639 ± 0.0026
F_p/F_*	0.00325 ± 0.00053	0.00384 ± 0.00046	0.00281 ± 0.00051
T_B (K)	1270 ± 190	1450 ± 230	1130 ± 160
F_* (mJy)	18.7884 ± 0.0069	18.7023 ± 0.0064	18.6155 ± 0.0068
F_p [b] (μJy)	61.1 ± 10.0	71.9 ± 8.6	52.3 ± 9.5

Notes.
[a] Jointly fit ephemeris, assuming a period of 3.5247455 days (Torres et al. 2008).
[b] Computed from the posterior MCMC distributions of F_* and F_p/F_*.

5.2. Results

The parameters for the fit in which $T_{c,e}$ and F_p/F_* are fit jointly across all eclipses (but F_* remains independent) are shown in Table 5, and parameters for the three wholly independent eclipse fits are shown in Table 6. The data, best-fit models, and residuals for all three eclipses and the combined data set are plotted in Figure 7. The only strong correlations apparent in the resulting posterior distributions are between F_* and F_p/F_*—expected since we are making a relative measurement. We show how the residuals to the combined fit bin down with increasing sample size in Figure 4: the residuals average down more slowly than the $N^{-1/2}$ expectation from uncorrelated errors. This indicates the presence of correlated (red) noise (see Pont et al. 2006) in these data, which is expected given the behavior of the eclipse residuals shown in Figure 7.

5.3. Discussion

The three eclipse depths have a dispersion of 13%, consistent with our estimated measurement errors (12%–18%). We thus find no evidence for variability of planetary emission, in good agreement with general circulation models which predict HD 209458b's MIR dayside emission will vary by <5% (e.g.,

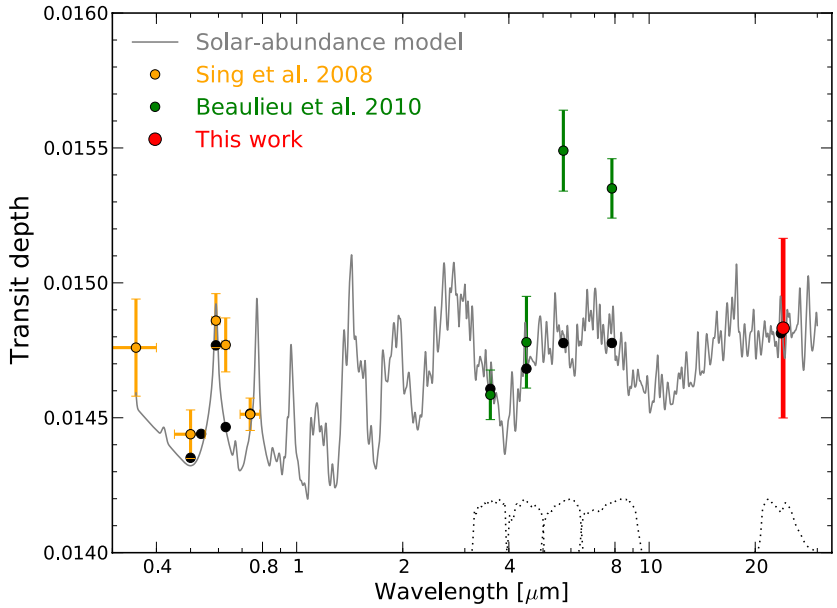

Figure 6. Measurements of the transit depth of HD 209458b: binned optical spectroscopy (Sing et al. 2008), previous mid-infrared photometry (Beaulieu et al. 2010), and our 24 μm measurement. The solid line is a model generated using the (dot-dashed) temperature–pressure profile shown in Figure 9. The solid black points without error bars represent the weighted averages of the model over the corresponding bandpasses (indicated at bottom).

(A color version of this figure is available in the online journal.)

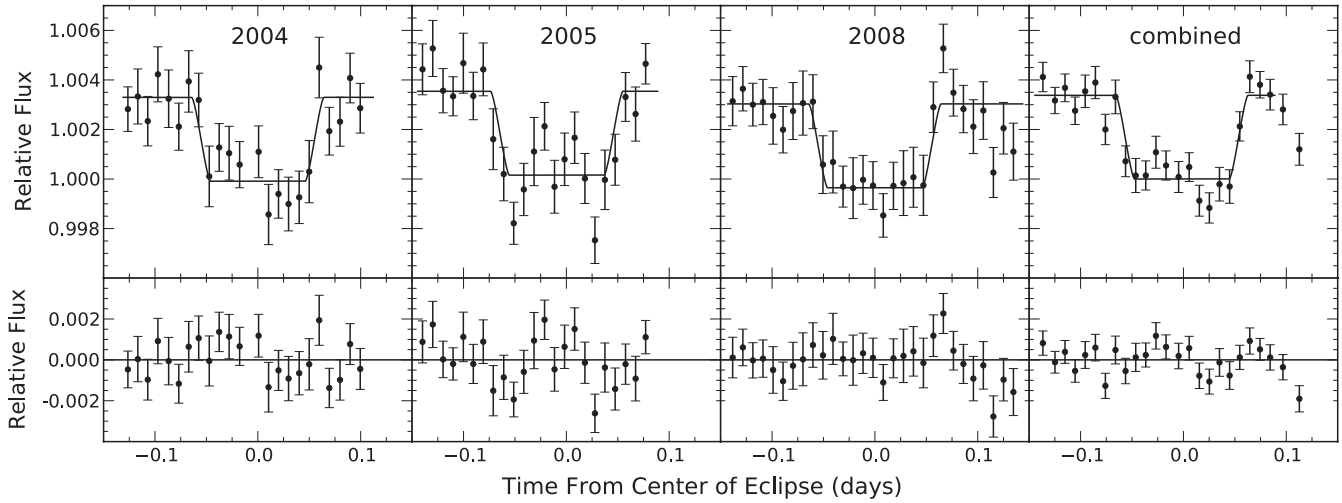

Figure 7. MIPS 24 μm eclipses of HD 209458b. The top panels show photometry and the best-fit models, and the lower panels show the residuals to the fits. For plotting purposes the data have been corrected for the MIPS 14-position sensitivity variations, normalized by the stellar flux, and binned by 70 points (for the individual eclipses) and by 210 points (for the combined data set).

Rauscher et al. 2008; Showman et al. 2009; Dobbs-Dixon et al. 2010) and consistent with the measurement that HD 189733b's 8 μm dayside emission varies by <2.7% (Agol et al. 2010). Our mean eclipse depth over all three epochs—0.338% ± 0.026%—is ∼1.3σ deeper than the initial measurement by Deming et al. (2005) of 0.26% ± 0.046%. We convert this eclipse depth to a brightness temperature of 1320 ± 80 K using the method outlined by C10.

We plot the ensemble of HD 209458b's secondary eclipse measurements in Figure 8 along with a model of planet/star contrast ratio versus wavelength. The modeling procedure is described in detail in Fortney et al. (2006, 2008). Using a stellar model for the incident flux and a solar metallicity atmosphere, we derive a radiative-convective pressure–temperature profile assuming chemical equilibrium mixing ratios. The model assumes no loss of absorbed energy to the night side, and redistribution of energy over the day side only (see Fortney et al. 2008). We show the pressure–temperature profile, which features a temperature inversion due to the absorption of stellar flux by TiO and VO gasses, in Figure 9. Clearly, a stronger temperature inversion is needed, as the contrast between the IRAC 3.6 and 4.5 μm bands is not large enough. Since the 24 μm photosphere is predicted to lie at 1–10 mbar on HD 209458b (Showman et al. 2009), our measurement indicates a somewhat cooler temperature than is expected for this planet given its atmospheric temperature inversion. The anomalously low 24 μm flux has been noted previously (e.g., Madhusudhan & Seager 2010); taken in concert with υ and b's large and still-unexplained 24 μm phase offset (C10), these results suggest that our current understanding of atmospheric opacity sources in this wavelength range may be incomplete. Alternatively, we can reasonably fit the 3.6, 8.0, and 24 μm points with the dayside emission of the three-dimensional general circulation model of Showman et al. (2009), which is cooler than the

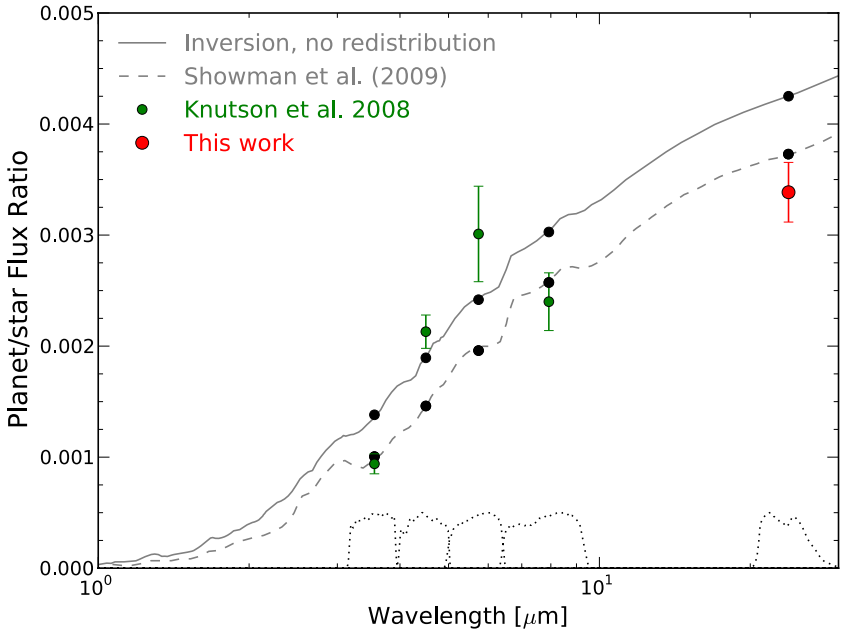

Figure 8. Measurements of the secondary eclipse depth of HD 209458b: previous *Spitzer*/IRAC photometry (Knutson et al. 2008) and our 24 μm measurement. The solid line is from a model assuming zero redistribution of incident flux and including gaseous TiO and VO to drive a temperature inversion; we show this model's temperature–pressure profile in Figure 9. The dashed line is the emission spectrum from Showman et al. (2009). The solid black points without error bars represent the weighted averages of the models over the corresponding bandpasses (indicated at bottom).

(A color version of this figure is available in the online journal.)

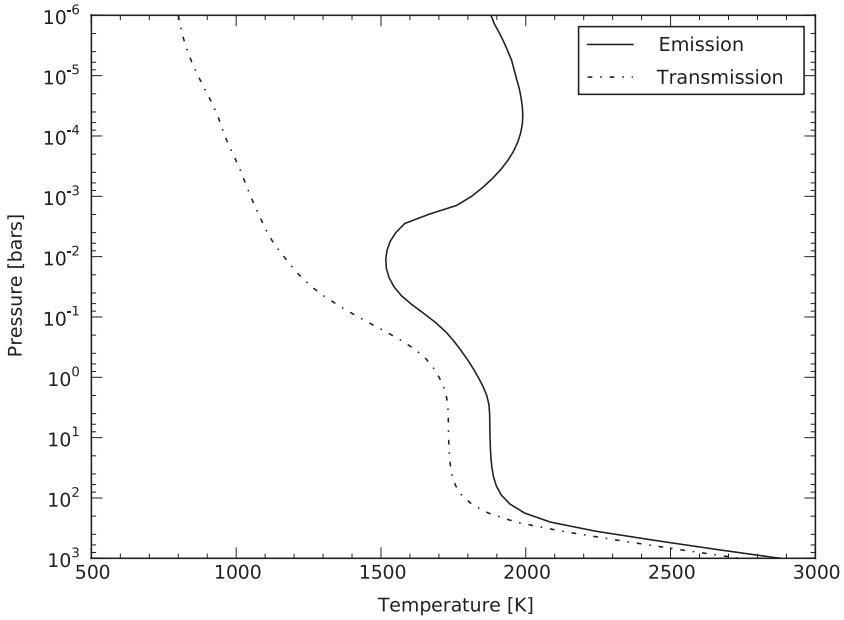

Figure 9. Temperature–pressure ($T-P$) profiles used to generate our model spectra. The dot-dashed curve is a planet-wide average $T-P$ profile taken from a full (4π) redistribution model, and is used to model the transmission spectrum shown in Figure 6. It includes TiO/VO opacity, but these species have only a minor effect since nearly all of the Ti/V has condensed out of the gas phase at these cooler temperatures. The solid curve is from a model assuming no redistribution of absorbed energy (making it hotter), and includes TiO/VO to drive the temperature inversion seen in Figure 8.

corresponding one-dimensional model from Fortney et al. (2008). Clearly, more work is needed to robustly fit the day-side photometry of the planet within the framework of a one-dimensional or three-dimensional self-consistent model.

We also fit a linear relation to the three eclipse times in the same manner as in Section 4. We compute a period of 3.5247445 ± 0.0000097 days, which differs from the established period (Torres et al. 2008) by 0.99×10^{-6} days (0.086 s), well within the uncertainties. This value also agrees with our measurement of the period from the transit fits; the two periods differ by only 0.79 ± 0.94 s, which is (as expected) consistent with zero.

6. JOINT ORBITAL CONSTRAINTS AND SYSTEM FLUX

6.1. Timing and Eccentricity: Still a Chance for Winds

Measuring the times of transit and secondary eclipse constrains the quantity $e\cos\omega$, where e is the planet's orbital eccentricity and ω its longitude of periastron (Seager 2011, chapter by J. Winn). We resample the posterior distributions of

$T_{c,t}$ and $T_{c,e}$ from the fits shown in Tables 2 and 5 and compute the difference between our transit and eclipse ephemerides (i.e., $[T_{c,e} - T_{c,t}] \bmod P - P/2$) to be 32 ± 129 s after also accounting for the 47 s light-travel time from the planet's location during eclipse to its location during transit (Torres et al. 2008). This results constrains $e \cos \omega$ to be 0.00004 ± 0.00033, consistent with zero and with previous constraints from radial velocity (Torres et al. 2008). We do not see the marginal timing offset previously reported (Knutson et al. 2008), which may have been biased by the higher level of correlated noise (due to the IRAC intrapixel effect) in the 3.6 and 4.5 μm IRAC data.

A measurement of $e \cos \omega$ directly constrains the apparent velocity offset that can be induced in planetary absorption lines during transit (see Montalto et al. 2011); this provides an independent check as to whether the recent measurement of a velocity offset of 2 ± 1 km s^{-1} in HD 209458b (Snellen et al. 2010) can be attributed to a low, but nonzero, orbital eccentricity. Our timing measurements of HD 209458b set a 3σ upper limit on any velocity offset due to the planet's orbital eccentricity of only 140 m s$^{-1}/(1 - e^2)^{-1/2}$. Thus, the claimed velocity offset, though still of low significance, cannot be dismissed as resulting from HD 209458b's orbital eccentricity.

6.2. System Flux: No Excess Detected

Although our primary science results—the transit and eclipse depths—rely on relative flux measurements, our observations also allow us to measure absolute 24 μm photometry for the HD 209458 system. Our flux measurements for this system vary from epoch to epoch by much more than our quoted statistical uncertainties, but the variations are not large compared to the $\lesssim$1% repeatability and 2% absolute calibration accuracy of the MIPS 24 μm array (Engelbracht et al. 2007). Our 21 pixel aperture encloses 99.2% of the starlight (as determined from our synthetic PSF), and we account for this small effect in the value quoted below.

We therefore report the 24 μm system flux as 18.7 ± 0.4 mJy, consistent with the flux expected from the HD 209458 stellar photosphere (as reported by Deming et al. 2005). HD 209458 was not detected by *IRAS* (Beichman et al. 1988), but is present in the *Wide-field Infrared Survey Explorer*'s (*WISE*) all-sky point-source catalog (Wright et al. 2010). The *WISE* photometry gives a W4 system flux of 25.74 ± 0.12 mJy, which is higher than, but marginally ($\sim 3\sigma$) consistent with, the *Spitzer*-derived value after accounting for the different wavelengths of the two instruments. We therefore conclude that HD 209458 does not have a strong 24 μm infrared excess, as is typical of middle-aged F dwarfs (Moór et al. 2011).

7. CONCLUSIONS AND FUTURE WORK

We have described a homogeneous analysis of all *Spitzer* MIPS observations of the hot Jupiter HD 209458b. The data comprise three eclipses, two and a half transits, and a long, continuous observation designed to observe the planet's thermal phase curve; of these, analysis of two of the eclipses, one transit, and the phase curve observations have remained unpublished until now. The long-duration phase curve observation exhibits a detector ramp that appears similar to the ramp seen in *Spitzer*/IRAC 8 μm photometry, and we model this effect using the exponential function proposed by Agol et al. (2010). We also see a $\sim -0.2\%$ flux decrease in the latter portion of the phase curve observations. This fallback is similar to a known (but poorly characterized) variation in the response of the MIPS detector when subjected to bright illumination (see Figure 2 and Young et al. 2003).

We are unable to determine why either the fallback or the ramp have not been seen in any prior MIPS observations. Despite this failure, the correspondence between our photometry and the pre-launch array calibration data leads us to conclude that ramp and fallback are correlated and both are most likely of instrumental, rather than astrophysical, origin. This conclusion is strengthened by the result that fitting periodic phase functions to the data yields a planetary model hotter on its night side than its day side, strikingly at odds with theory (Rauscher et al. 2008; Showman et al. 2009; Dobbs-Dixon et al. 2010; Cowan & Agol 2011a) and inconsistent with other published observations of hot Jupiters (Harrington et al. 2006; Knutson et al. 2007, 2009b; Crossfield et al. 2010).

We see no evidence for variation in the three eclipse depths, and a joint fit of all three eclipses gives our best estimate of the 24 μm planet/star contrast: $0.338\% \pm 0.026\%$. This value is more precise and higher than the previously published measurement (Deming et al. 2005), and corresponds to an average dayside brightness temperature of 1320 ± 80 K, consistent with models of this planet's thermal atmospheric structure (Showman et al. 2009; Madhusudhan & Seager 2010; Moses et al. 2011). We note parenthetically that this new eclipse depth has already diffused into several papers (see Showman et al. 2009; Burrows et al. 2010; Madhusudhan & Seager 2009, 2010; Fortney et al. 2010; Moses et al. 2011); the value and uncertainty quoted in those works are close to those we report here, so their conclusions should be relatively unaffected.

We see no evidence for variations in our transit measurements, and a joint fit of our two and a half transits yields a 24 μm transit depth of $1.484\% \pm 0.033\%$. The transit depth is less well constrained than the eclipse depth because only half of the first transit was observed, and the last transit occurred during the detector ramp.

The ephemerides calculated from our analyses of the transits and eclipses allow us to compute orbital periods of 3.5247537 ± 0.0000049 days and 3.5247445 ± 0.0000097 days, respectively, which are consistent with but less precise than the orbital period of Torres et al. (2008). Eclipses occur 32 ± 129 s earlier than would be expected from a circular orbit, which constrains the orbital quantity $e \cos \omega$ to be 0.00004 ± 0.00033. This suggests that HD 209458b's inflated radius (larger than predicted by models of planetary interiors; Fortney et al. 2007) cannot be explained by interior heating from ongoing tidal circularization, and that the possible velocity offset reported by Snellen et al. (2010) cannot be explained by a nonzero orbital eccentricity.

Although we obtain improved estimates of the 24 μm transit and secondary eclipse parameters, instrumental effects prevent a conclusive detection of the planet's thermal phase curve. The phase curve signal is inextricably combined with the systematic fallback effect, despite estimates that the planet's day/night contrast should be as large as a few parts per thousand (Showman et al. 2009). Such a large and intermittent systematic effect has profound implications for future mid-infrared exoplanet observations with *EChO*, *SPICA*, and *JWST*. Models of terrestrial planet phase curves predict phase amplitudes of $\lesssim 10^{-4}$ (Selsis et al. 2011; Maurin et al. 2012); such observations could be utterly confounded by the instrumental systematics seen in our observations, and so may be much more challenging that has been heretofore assumed (Kaltenegger & Traub 2009; Seager & Deming 2009). Although it may be possible to reduce

the effect of the ramp with a pre-flash strategy similar to that adopted for the 8 μm IRAC array, a further defense against these challenges would seem to be a more comprehensive campaign of array characterization. Specifically, a detailed characterization of the detector response to sustained levels of the high illumination expected from observations of terrestrial planets around the brightest nearby stars is highly desirable, and should be considered an essential requirement for all future infrared space telescopes.

We thank Brad Hansen for many informative discussions, and Alberto Noriega-Crespo and James Colbert of the Spitzer Science Center for discussions about calibration of, and systematics in, MIPS 24 μm photometry. We thank the referee for useful comments and the suggestion to expand our discussion of the residual noise properties.

This work is based on observations made with the *Spitzer Space Telescope*, which is operated by the Jet Propulsion Laboratory, the California Institute of Technology under a contract with NASA. Support for this work was provided by NASA through an award issued by JPL/Caltech. We received free software and services from SciPy, Matplotlib, and the Python Programming Language. This research made use of Tiny Tim/Spitzer, developed by John Krist for the Spitzer Science Center; the Center is managed by the California Institute of Technology under a contract with NASA.

REFERENCES

Agol, E., Cowan, N. B., Knutson, H. A., et al. 2010, ApJ, 721, 1861
Baines, E. K., McAlister, H. A., ten Brummelaar, T. A., et al. 2008, ApJ, 680, 728
Beaulieu, J. P., Kipping, D. M., Batista, V., et al. 2010, MNRAS, 409, 963
Beichman, C. A., Neugebauer, G., Habing, H. J., et al. 1988, Infrared Astronomical Satellite (IRAS) Catalogs and Atlases, Vol. 1: Explanatory Supplement (Pasadena: California Institute of Technology), 1
Bouchy, F., Udry, S., Mayor, M., et al. 2005, A&A, 444, L15
Brown, T. M., Charbonneau, D., Gilliland, R. L., Noyes, R. W., & Burrows, A. 2001, ApJ, 552, 699
Burke, C. J., McCullough, P. R., Valenti, J. A., et al. 2007, ApJ, 671, 2115
Burrows, A., Budaj, J., & Hubeny, I. 2008, ApJ, 678, 1436
Burrows, A., Hubeny, I., Budaj, J., & Hubbard, W. B. 2007, ApJ, 661, 502
Burrows, A., Rauscher, E., Spiegel, D. S., & Menou, K. 2010, ApJ, 719, 341
Charbonneau, D., Allen, L. E., Megeath, S. T., et al. 2005, ApJ, 626, 523
Charbonneau, D., Brown, T. M., Latham, D. W., & Mayor, M. 2000, ApJ, 529, L45
Charbonneau, D., Brown, T. M., Noyes, R. W., & Gilliland, R. L. 2002, ApJ, 568, 377
Charbonneau, D., Knutson, H. A., Barman, T., et al. 2008, ApJ, 686, 1341
Cho, J. Y.-K., Menou, K., Hansen, B. M. S., & Seager, S. 2003, ApJ, 587, L117
Cho, J. Y.-K., Menou, K., Hansen, B. M. S., & Seager, S. 2008, ApJ, 675, 817
Colbert, J. (ed.) 2011, MIPS Instrument Handbook, v3.0, Spitzer Science Center (Pasadena: SSC)
Cooper, C. S., & Showman, A. P. 2005, ApJ, 629, L45
Cowan, N. B., & Agol, E. 2011a, ApJ, 726, 82
Cowan, N. B., & Agol, E. 2011b, ApJ, 729, 54
Cowan, N. B., Agol, E., & Charbonneau, D. 2007, MNRAS, 379, 641
Crossfield, I. J. M., Hansen, B. M. S., Harrington, J., et al. 2010, ApJ, 723, 1436
Deming, D., Harrington, J., Seager, S., & Richardson, L. J. 2006, ApJ, 644, 560
Deming, D., Seager, S., Richardson, L. J., & Harrington, J. 2005, Nature, 434, 740
Désert, J.-M., Vidal-Madjar, A., Lecavelier Des Etangs, A., et al. 2008, A&A, 492, 585
Dobbs-Dixon, I., Cumming, A., & Lin, D. N. C. 2010, ApJ, 710, 1395
Eastman, J., Siverd, R., & Gaudi, B. S. 2010, PASP, 122, 935
Engelbracht, C. W., Blaylock, M., Su, K. Y. L., et al. 2007, PASP, 119, 994
Fortney, J. J., Cooper, C. S., Showman, A. P., Marley, M. S., & Freedman, R. S. 2006, ApJ, 652, 746
Fortney, J. J., Lodders, K., Marley, M. S., & Freedman, R. S. 2008, ApJ, 678, 1419
Fortney, J. J., Marley, M. S., & Barnes, J. W. 2007, ApJ, 659, 1661
Fortney, J. J., Shabram, M., Showman, A. P., et al. 2010, ApJ, 709, 1396
Harrington, J., Hansen, B. M., Luszcz, S. H., et al. 2006, Science, 314, 623
Heim, G. B., Henderson, M. L., Macfeely, K. I., et al. 1998, Proc. SPIE, 3356, 985
Heng, K., Frierson, D. M. W., & Phillipps, P. J. 2011a, MNRAS, 418, 2669
Heng, K., Menou, K., & Phillipps, P. J. 2011b, MNRAS, 413, 2380
Henry, G. W., Marcy, G. W., Butler, R. P., & Vogt, S. S. 2000, ApJ, 529, L41
Kaltenegger, L., & Traub, W. A. 2009, ApJ, 698, 519
Knutson, H. A., Charbonneau, D., Allen, L. E., Burrows, A., & Megeath, S. T. 2008, ApJ, 673, 526
Knutson, H. A., Charbonneau, D., Allen, L. E., et al. 2007, Nature, 447, 183
Knutson, H. A., Charbonneau, D., Cowan, N. B., et al. 2009a, ApJ, 703, 769
Knutson, H. A., Charbonneau, D., Cowan, N. B., et al. 2009b, ApJ, 690, 822
Knutson, H. A., Howard, A. W., & Isaacson, H. 2010, ApJ, 720, 1569
Knutson, H. A., Madhusudhan, N., Cowan, N. B., et al. 2011, ApJ, 735, 27
Madhusudhan, N., Harrington, J., Stevenson, K. B., et al. 2011a, Nature, 469, 64
Madhusudhan, N., Mousis, O., Johnson, T. V., & Lunine, J. I. 2011b, ApJ, 743, 191
Madhusudhan, N., & Seager, S. 2009, ApJ, 707, 24
Madhusudhan, N., & Seager, S. 2010, ApJ, 725, 261
Mandel, K., & Agol, E. 2002, ApJ, 580, L171
Maurin, A. S., Selsis, F., Hersant, F., & Belu, A. 2012, A&A, 538, A95
Mayor, M., & Queloz, D. 1995, Nature, 378, 355
Mazeh, T., Naef, D., Torres, G., et al. 2000, ApJ, 532, L55
Montalto, M., Santos, N. C., Boisse, I., et al. 2011, A&A, 528, L17
Moór, A., Naef, D., Torres, G., et al. 2011, ApJS, 193, 4
Moses, J. I., Visscher, C., Fortney, J. J., et al. 2011, ApJ, 737, 15
Pont, F., Zucker, S., & Queloz, D. 2006, MNRAS, 373, 231
Rauscher, E., & Menou, K. 2010, ApJ, 714, 1334
Rauscher, E., & Menou, K. 2012, ApJ, 745, 78
Rauscher, E., Menou, K., Cho, J., Seager, S., & Hansen, B. M. S. 2008, ApJ, 681, 1646
Richardson, L. J., Deming, D., & Seager, S. 2003, ApJ, 597, 581
Richardson, L. J., Harrington, J., Seager, S., & Deming, D. 2006, ApJ, 649, 1043
Rieke, G. H., Young, E. T., Cadien, J., et al. 2004, Proc. SPIE, 5487, 50
Rowe, J. F., Matthews, J. M., Seager, S., et al. 2008, ApJ, 689, 1345
Schuler, S. C., Flateau, D., Cunha, K., et al. 2011, ApJ, 732, 55
Seager, S. 2011, in Exoplanets, ed. S. Piper (Tucson, AZ: Univ. Arizona Press)
Seager, S., & Deming, D. 2009, ApJ, 703, 1884
Seager, S., & Sasselov, D. D. 2000, ApJ, 537, 916
Selsis, F., Wordsworth, R. D., & Forget, F. 2011, A&A, 532, A1
Shabram, M., Fortney, J. J., Greene, T. P., & Freedman, R. S. 2011, ApJ, 727, 65
Showman, A. P., Fortney, J. J., Lian, Y., et al. 2009, ApJ, 699, 564
Showman, A. P., & Guillot, T. 2002, A&A, 385, 166
Sing, D. K., Désert, J., Lecavelier Des Etangs, A., et al. 2009, A&A, 505, 891
Sing, D. K., Vidal-Madjar, A., Lecavelier des Etangs, A., et al. 2008, ApJ, 686, 667
Snellen, I. A. G., de Kok, R. J., de Mooij, E. J. W., & Albrecht, S. 2010, Nature, 465, 1049
Southworth, J. 2008, MNRAS, 386, 1644
Spiegel, D. S., Silverio, K., & Burrows, A. 2009, ApJ, 699, 1487
Stevenson, K. B., Harrington, J., Nymeyer, S., et al. 2010, Nature, 464, 1161
Thrastarson, H. T., & Cho, J. Y.-K. 2010, ApJ, 716, 144
Torres, G., Winn, J. N., & Holman, M. J. 2008, ApJ, 677, 1324
von Braun, K., van Belle, G. T., Ciardi, D. R., et al. 2008, ApJ, 677, 545
Wright, E. L., Eisenhardt, P. R. M., Mainzer, A. K., et al. 2010, AJ, 140, 1868
Young, E. T., Rieke, G. H., Cadien, J., et al. 2003, Proc. SPIE, 4850, 98